# Comparative Performance Analysis of Vector Control, Fuzzy Logic Control, and Adaptive Quantum Fuzzy Logic for Induction Motor Drives in Hybrid Renewable Energy Systems

Mouhamadou Moustapha Diop *, Adam W. Skorek *, Modou Diop *

Posted Date: 20 May 2026

doi: 10.20944/preprints202605.1382.v1

Keywords: induction motor; vector control; fuzzy logic control; adaptive quantum fuzzy logic; hybrid renewable energy systems; thermoradiative cells; THD reduction; renewable energy drives

 doi:10.20944/preprints202605.1382.v1



*Article*

# Comparative Performance Analysis of Vector Control, Fuzzy Logic Control, and Adaptive Quantum Fuzzy Logic for Induction Motor Drives in Hybrid Renewable Energy Systems

**Mouhamadou Moustapha Diop *, Adam W. Skorek * and Modou Diop ***

Université du Québec à Trois-Rivières, Trois-Rivieres, Canada

* Correspondence: mouhamadou.moustapha.diop@uqtr.ca (M.M.D.); adam.skrek@uqtr.ca (A.W.S.); modou.diop@uqtr.ca (M.D.)

**Abstract**

This paper presents an Adaptive Quantum Fuzzy Logic (ALFQ) control strategy applied to an induction motor (IM) supplied by a hybrid renewable energy system integrating photovoltaic (PV), wind, and thermoradiative (TR) energy sources. Conventional Vector Control (VC) and classical Fuzzy Logic Control (FLC) approaches are not fully developed in this study; instead, their main limitations and performances reported in the literature are used as comparative references in order to focus on the proposed quantum-based control strategy. The main objective is to investigate the dynamic response, robustness against parameter uncertainties, harmonic performance, and adaptability of the proposed ALFQ controller under varying operating conditions. The ALFQ approach combines fuzzy inference mechanisms with quantum-inspired optimization algorithms capable of automatically adjusting the membership functions and minimizing the speed tracking error. Simulation results obtained under MATLAB/Simulink demonstrate that the proposed ALFQ controller significantly improves the dynamic behavior of the induction motor drive. The obtained results show fast response time, quasi-zero overshoot, negligible steady-state error, reduced current ripple, and lower Total Harmonic Distortion (THD). The controller also exhibits excellent robustness against rapid load disturbances, rotor resistance variations, and nonlinear operating conditions. A comparative analysis based on literature results confirms that the proposed ALFQ strategy outperforms conventional VC and classical FLC approaches in terms of tracking accuracy, robustness, harmonic reduction, and global dynamic stability. These results demonstrate the effectiveness of quantum-inspired fuzzy optimization for high-performance induction motor drives supplied by hybrid renewable energy systems.

**Keywords:** induction motor; vector control; fuzzy logic control; adaptive quantum fuzzy logic; hybrid renewable energy systems; thermoradiative cells; THD reduction; renewable energy drives

## I. Introduction

Recent advances in renewable energy systems and intelligent electrical drives have significantly increased the interest in hybrid renewable energy architectures for industrial applications. Induction motors (IMs) remain the most widely used electrical machines because of their robustness, reliability, and reduced maintenance requirements. However, modern industrial systems require advanced control strategies capable of ensuring high dynamic performance, robustness against parameter uncertainties, and low harmonic distortion under variable operating conditions [1] [2][3].

 doi:10.20944/preprints202605.1382.v1



Conventional photovoltaic (PV) and wind energy systems are widely used in renewable electrical drive applications. Nevertheless, these sources remain highly dependent on climatic conditions and solar irradiation. Consequently, thermoradiative (TR) cells have recently emerged as promising complementary energy conversion devices capable of generating electrical power from infrared thermal radiation during nighttime conditions and low-grade heat recovery applications [4][5]. Unlike photovoltaic cells, thermoradiative devices operate through radiative emission toward a colder environment and strongly depend on low-bandgap semiconductor materials. Several studies demonstrated the potential of materials such as InSb, InAs, HgCdTe, and InAs/GaSb superlattices for thermoradiative energy conversion [4,6,7]. Recent investigations also highlighted the importance of very low bandgap molecular families such as SnSbX and SnAsX compounds for future high efficiency thermoradiative devices [7]. To ensure stable operation of induction motor drives supplied by hybrid renewable energy systems integrating PV, wind, and TR sources, advanced control techniques become essential. Classical Vector Control (VC), initially proposed by Hasse in 1969 and later generalized by Blaschke in 1972, remains one of the most widely used control strategies because of its effective flux–torque decoupling capability [8], [9]. However, VC remains highly sensitive to machine parameter variations, especially rotor resistance variations caused by thermal effects.To overcome these limitations, Fuzzy Logic Control (FLC) has been extensively investigated due to its robustness against nonlinearities and parameter uncertainties [10]. More recently, adaptive and quantum-inspired optimization methods have attracted increasing interest for intelligent electrical drive applications. In this context, Adaptive Quantum Fuzzy Logic (ALFQ) combines the robustness of fuzzy logic with probabilistic quantum optimization mechanisms capable of automatically adjusting the membership functions and minimizing the tracking error.

Table I summarizes the main limitations of conventional vector control strategies commonly reported in the literature for induction motor drives. Direct Field Oriented Control (DFOC) and Indirect Field Oriented Control (IFOC) provide efficient flux–torque decoupling and satisfactory dynamic performance under nominal operating conditions. However, these approaches remain strongly dependent on accurate machine parameter estimation, particularly rotor resistance and rotor time constant variations. Their performances may significantly degrade under thermal effects, parameter uncertainties, magnetic saturation, and severe transient operating conditions.

**Table 1.** Main limitations of conventional vector control and fuzzy-based control strategies for induction motor drives.

| Approach | Principle / Explanation | References | Main Limitations |
|---|---|---|---|
| DFOC (Direct Field Oriented Control) | Direct measurement or estimation of the rotor flux vector in both magnitude and angular position. This method ensures precise flux orientation and efficient flux–torque decoupling, including during transient operation. | [11] | - Direct flux measurement is unreliable in industrial environments<br>- High sensitivity to measurement noise<br>- Filtering requirements may slow the dynamic response<br>- Thermal effects and magnetic saturation<br>- High hardware cost |
| IFOC (Indirect Field Oriented Control) | Indirect estimation of the rotor flux using the motor model, stator currents, applied voltages, and rotor speed. This approach avoids flux sensors | [12] | - Sensitivity to rotor resistance (Rr) variations<br>- Dependence on rotor time constant (Tr)<br>- Magnetic saturation effects |

 doi:10.20944/preprints202605.1382.v1



| | | | |
|---|---|---|---|
| | and facilitates industrial implementation. | | - Progressive flux misalignment<br>- Torque and speed oscillations, especially at low speed |
| Classical Vector Control Strategies | Approaches based on the mathematical model of the motor allowing the induction machine to operate as a flux–torque decoupled system in order to improve torque and speed dynamics. | [10]–[12] | - Strong dependence on the motor model<br>- Assumption of linear and invariant parameters<br>- Performance degradation under variable loads and severe transients<br>- Complexity related to observers and estimators |
| Vector Control Combined with Fuzzy Logic | Integration of linguistic rules and membership functions to improve control robustness against nonlinearities, parameter uncertainties, and load variations. | [13,14] | - Dependence on human expertise<br>- Difficult selection of membership functions<br>- More difficult formal validation<br>- Real-time implementation complexity depending on architecture<br>- Limited capability to manage strongly nonlinear and dynamic phenomena |

To improve robustness against nonlinearities and load disturbances, several studies have proposed integrating fuzzy logic techniques with vector control strategies. Although fuzzy-based approaches improve adaptability and disturbance rejection capability, their performances still depend on heuristic tuning procedures and the appropriate selection of membership functions and inference rules.

For these reasons, recent research efforts have increasingly focused on intelligent and adaptive control approaches capable of automatically optimizing the controller parameters under varying operating conditions. In this context, the proposed Adaptive Quantum Fuzzy Logic (ALFQ) controller aims to overcome the limitations of conventional VC and classical FLC approaches by combining fuzzy inference with quantum-inspired optimization mechanisms to improve dynamic response, robustness, and tracking accuracy.

Therefore, this paper presents a comparative analysis of Vector Control, Fuzzy Logic Control, and Adaptive Quantum Fuzzy Logic applied to an induction motor supplied by a hybrid renewable energy system integrating photovoltaic, wind, and thermoradiative energy sources. The comparative study focuses on dynamic response, robustness, harmonic distortion, current quality, and adaptability under varying operating conditions.

Therefore, in order to ensure continuous and efficient operation of the induction motor under varying environmental and loading conditions, a hybrid renewable energy architecture combining photovoltaic, wind, and thermoradiative energy sources is proposed in this work. The generated energy is regulated through a common DC bus and supplied to the induction motor via a three-level inverter structure. The proposed system integrates advanced control strategies, including Vector Control (VC), Fuzzy Logic Control (FLC), and Adaptive Quantum Fuzzy Logic (ALFQ), in order to evaluate their dynamic performance, robustness against parameter uncertainties, harmonic behavior, and adaptability under hybrid renewable operating conditions. The overall architecture of the proposed hybrid renewable energy system and induction motor drive is illustrated in Figure 1.

 doi:10.20944/preprints202605.1382.v1



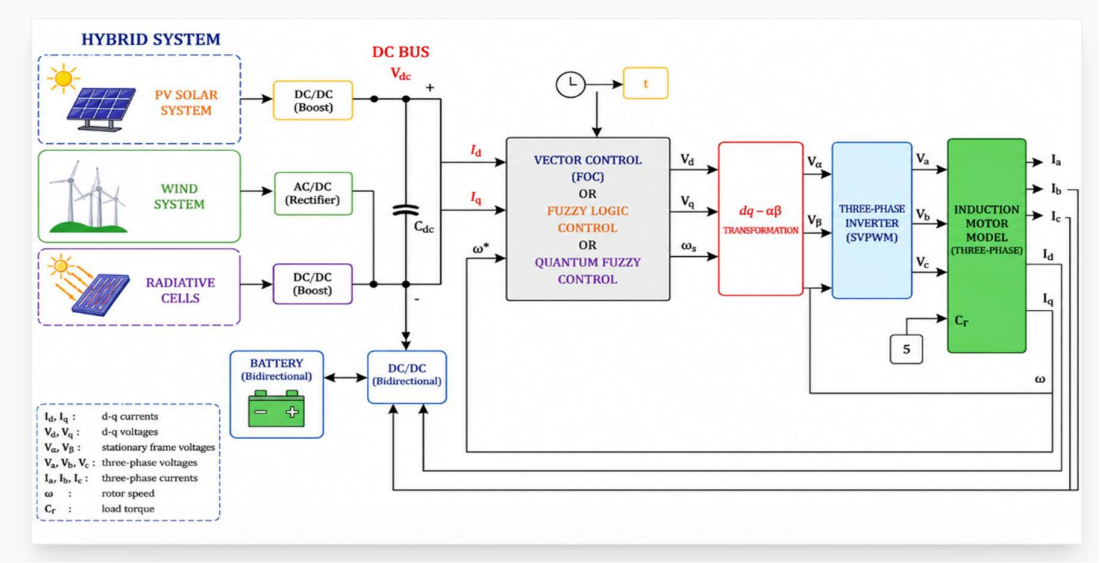


**Figure 1.** Proposed hybrid renewable energy powered induction motor drive architecture based on VC, FLC, and ALFQ control strategies.

## II. Hybrid Renewable Energy System Architecture

*A. Model of the PV System*

The PV panel can be represented by the equivalent electrical circuit shown in Figure 2. It consists of a current source connected in parallel with a diode. The current generated by the photovoltaic cell, $I_{PV}$, can therefore be expressed as follows.

By applying Kirchhoff's current law, the following equation is obtained:

$$I_{PV} = I_{Ph} - I_d$$

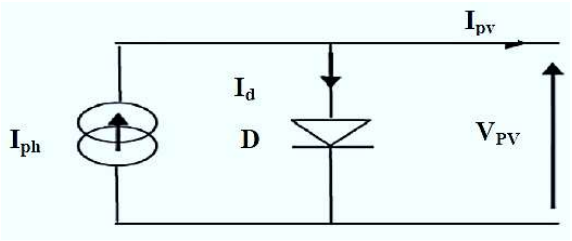


**Figure 2.** Single-diode equivalent electrical model of the photovoltaic cell.

For an ideal PV generator, the voltage at the diode terminals is equal to:

$$V_{PV} = V_d$$

$V_d$: voltage of the diode.

The diode being a non-linear element, its characteristic I-V is given by the relation:

$$I_d = I_0 \ . \ e^{q.V_{PV}/AKT} - 1 \qquad (2)$$

$I_0$: The saturation current of the right, which is expressed as:

$$\left\{ I_0 = I_0(T1).\left(\frac{T}{T1}\right)^{3/n}.\ e^{q.E_g/AK\left(\frac{1}{T}-\frac{1}{T1}\right)} \right\} \qquad (3)$$

with

$$I_0(T1) = I_{sc}(T1)/\ e^{q.V_{oc}(T1)/AK} \ - 1$$

 doi:10.20944/preprints202605.1382.v1



with $E_g$: Diode Threshold Voltage $= 1.12ev$; $I_{SC}$: Short-circuit current; $V_{OC}$: open circuit voltage; q: Electric charge that is equal to 1.6x10 $e^{-19}$C; K: Boltzmann constant (K = 1,3854x 10$e^{-23}$J/K; A: diode quality factor; KT/q: the thermal potential; T1: Temperature at time T1; T2: Temperature at time T2; $I_{Ph}$: Photonic current of the diode which is given by the following relation:

$$\boldsymbol{I_{Ph} = I_{Ph}(T1).(1 + K_0.(T - T1))} \quad (4)$$

$$\textit{Avec } \boldsymbol{K_0 = I_{sc}(T2) - I_{sc}(T1)/(T2 - T1)}$$

*Then*

$$\boldsymbol{I_{PV} = I_{Ph} - I_0 .(e^{q.\frac{V_{PV}}{AKT}} - 1)} \quad (5)$$

$$I_{PV} = I_{Ph}(T1).(1 + K_0.(T - T1) - I_0 .(e^{q.V_{PV}/AKT} - 1) \quad (6)$$

*B. Model of the TR System*

The radiative flux emitted by the cell follows Plank's law while if a plane cell emits on a hemisphere:

$$\boldsymbol{\phi_c}(\Delta\mu) = \frac{2\pi}{h^3C^2} \int_{E_g}^{\infty} \boldsymbol{\eta_{extr}}(E)\, \varepsilon(E) \times \frac{E^2}{e^{\frac{E-\Delta\mu}{K_B T_c}} - 1}\, dE \quad (7)$$

where h: plank constant; C: the speed of light; $\eta_{extr}$: the efficiency of radiation extraction from the cell; E: the energy of the cell; $E_g$: the energy-restricted band of the cellular material; $K_B$: Boltzmann constant; $T_c$: Temperature of the cell.

The radiation flux absorbed by the cell is given by the same similar reasoning.

$$\boldsymbol{\phi_a}(\Delta\mu) = \frac{2\pi}{h^3C^2} \int_{E_g}^{\infty} \boldsymbol{\eta_{EQE}}(E)\, \varepsilon(E) \times \frac{E^2}{e^{\frac{E-\Delta\mu}{K_B T_a}} - 1}\, dE \quad (8)$$

where $\eta_{EQE}$: the external quantum efficiency of the cell; $T_a$: the ambient temperature.

The parameters in (7) represent the radiative and non-radiative process for a conventional diode with a current flux corresponding to the decrease of the radiation flux absorbed by the environment compared to the flux emitted with zero electrochemical potential (short circuit current).

For a sufficiently large bandgap energy $(E_g > 3kT)$, the current–voltage $(J–V)$characteristic can be approximated using the Shockley relation. Mathematically, it can be expressed as follows:

$$J(\Delta\mu) = \boldsymbol{J_{0,rad}}(\boldsymbol{e^{q\Delta\mu/K_B T_c} - 1}) + \boldsymbol{J_{0,nr}}(\boldsymbol{e^{q\Delta\mu/nK_B T_c} - 1}) + \boldsymbol{J_{sc}} \quad (9)$$

*C-Level Inverter Vector Control*

We can divide the vector control process into 3 steps:

Step1. Determination of $V_\alpha$; $V_\beta$; $V_{ref}$ and angle $\alpha$

**Table 2.** DETERMINATION OF SWITCHING TIMES T_A, T_B, AND T_C BY SECTORS AND REGIONS.

| | Region 1 | Region 2 | Region 3 | Region 4 |
|---|---|---|---|---|
| Sector 1 | $T_a = mT_m \sin\left(\frac{\pi}{3} - \theta\right)$<br>$T_b = T_m\left(1 - m\sin\left(\theta + \frac{\pi}{3}\right)\right)$<br>$T_c = mT_m \sin\theta$ | $T_a = T_m\left(2 - m\sin\left(\theta + \frac{\pi}{3}\right)\right)$<br>$T_b = mT_m \sin\theta$<br>$T_c = T_m\left(m\sin\left(\frac{\pi}{3} - \theta\right) - 1\right)$ | $T_a = T_m(1 - m\sin\theta)$<br>$T_b = T_m\left(m\sin\left(\frac{\pi}{3} + \theta\right) - 1\right)$<br>$T_c = T_m\left(m\sin\left(\theta - \frac{\pi}{3}\right) + 1\right)$ | $T_a = T_m(m\sin\theta - 1)$<br>$T_b = mT_m \sin\left(\frac{\pi}{3} - \theta\right)$<br>$T_c = T_m\left(2 - m\sin\left(\frac{\pi}{3} + \theta\right)\right)$ |

 doi:10.20944/preprints202605.1382.v1



| | | | | |
|---|---|---|---|---|
| Sector 2 | $T_a = mT_m \sin\left(\theta - \frac{\pi}{3}\right)$<br>$T_b = T_m(1 - m\sin\theta)$<br>$T_c = mT_m \sin\left(\frac{\pi}{3} + \theta\right)$ | $T_a = T_m\left(m\sin\left(\theta + \frac{\pi}{3}\right) - 1\right)$<br>$T_b = mT_m \sin\left(\theta - \frac{\pi}{3}\right)$<br>$T_c = T_m(2 - m\sin\theta)$ | $T_a = T_m\left(1 - m\sin\left(\theta + \frac{\pi}{3}\right)\right)$<br>$T_b = T_m(m\sin\theta - 1)$<br>$T_c = T_m\left(1 - m\sin\left(\theta - \frac{\pi}{3}\right)\right)$ | $T_a = T_m(2 - m\sin\theta)$<br>$T_b = mT_m \sin\left(\frac{\pi}{3} + \theta\right)$<br>$T_c = T_m\left(m\sin\left(\theta - \frac{\pi}{3}\right) - 1\right)$ |
| Sector3 | $T_a = mT_m \sin\theta$<br>$T_b = T_m\left(1 - m\sin\left(\theta - \frac{\pi}{3}\right)\right)$<br>$T_c = -mT_m \sin\left(\frac{\pi}{3} + \theta\right)$ | $T_a = T_m\left(2 - m\sin\left(\theta - \frac{\pi}{3}\right)\right)$<br>$T_b = mT_m \sin\left(\theta + \frac{\pi}{3}\right)$<br>$T_c = T_m(m\sin\theta - 1)$ | $T_a = T_m\left(1 + m\sin\left(\theta + \frac{\pi}{3}\right)\right)$<br>$T_b = T_m\left(m\sin\left(\theta - \frac{\pi}{3}\right) - 1\right)$<br>$T_c = T_m(1 - m\sin\theta)$ | $T_a = -T_m\left(1 + m\sin\left(\theta + \frac{\pi}{3}\right)\right)$<br>$T_b = mT_m \sin\theta$<br>$T_c = T_m\left(2 - m\sin\left(\theta - \frac{\pi}{3}\right)\right)$ |
| Sector 4 | $T_a = -mT_m \sin\theta$<br>$T_b = T_m\left(1 + m\sin\left(\theta + \frac{\pi}{3}\right)\right)$<br>$T_c = mT_m \sin\left(\theta - \frac{\pi}{3}\right)$ | $T_a = T_m\left(m\sin\left(\theta - \frac{\pi}{3}\right) - 1\right)$<br>$T_b = -mT_m \sin\theta$<br>$T_c = T_m\left(2 + m\sin\left(\theta + \frac{\pi}{3}\right)\right)$ | $T_a = T_m\left(1 - m\sin\left(\theta - \frac{\pi}{3}\right)\right)$<br>$T_b = -T_m\left(1 + m\sin\left(\theta + \frac{\pi}{3}\right)\right)$<br>$T_c = T_m(1 + m\sin\theta)$ | $T_a = T_m\left(2 + m\sin\left(\theta + \frac{\pi}{3}\right)\right)$<br>$T_b = mT_m \sin\left(\theta - \frac{\pi}{3}\right)$<br>$T_c = -T_m(1 - m\sin\theta)$ |
| Sector 5 | $T_a = -mT_m \sin\left(\frac{\pi}{3} + \theta\right)$<br>$T_b = T_m(1 + m\sin\theta)$<br>$T_c = mT_m \sin\left(\frac{\pi}{3} - \theta\right)$ | $T_a = T_m(2 + m\sin\theta)$<br>$T_b = mT_m \sin\left(\frac{\pi}{3} - \theta\right)$<br>$T_c = -T_m\left(1 + m\sin\left(\theta + \frac{\pi}{3}\right)\right)$ | $T_a = T_m\left(1 + m\sin\left(\theta - \frac{\pi}{3}\right)\right)$<br>$T_b = -T_m(1 + m\sin\theta)$<br>$T_c = T_m\left(1 + m\sin\left(\theta + \frac{\pi}{3}\right)\right)$ | $T_a = T_m\left(m\sin\left(\frac{\pi}{3} - \theta\right) - 1\right)$<br>$T_b = -mT_m \sin\left(\frac{\pi}{3} + \theta\right)$<br>$T_c = T_m(2 + m\sin\theta)$ |
| Sector 6 | $T_a = mT_m \sin\left(\theta + \frac{\pi}{3}\right)$<br>$T_b = T_m\left(1 + m\sin\left(\theta - \frac{\pi}{3}\right)\right)$<br>$T_c = -mT_m \sin\theta$ | $T_a = -T_m(1 + m\sin\theta)$<br>$T_b = mT_m \sin\left(\frac{\pi}{3} + \theta\right)$<br>$T_c = T_m\left(2 + m\sin\left(\theta - \frac{\pi}{3}\right)\right)$ | $T_a = T_m(1 + m\sin\theta)$<br>$T_b = T_m\left(m\sin\left(\frac{\pi}{3} - \theta\right) - 1\right)$ | $T_a = T_m\left(2 + m\sin\left(\theta - \frac{\pi}{3}\right)\right)$<br>$T_b = -mT_m \sin\theta$ |

 doi:10.20944/preprints202605.1382.v1



| | |
|---|---|
| $T_c = T_m\left(1 - m\sin\left(\theta + \frac{\pi}{3}\right)\right)$ | $T_c = T_m\left(m\sin\left(\theta + \frac{\pi}{3}\right) - 1\right)$ |

**Table 3.** DETERMINATION OF SWITCHING TIMES.

| | Time | Region 1 | Region 2 | Region 3 | Region 4 |
|---|---|---|---|---|---|
| Sector 1 | $T_{K_{a1}}$ | $T_a/2 + T_c/2 + T_b/3$ | $T_b + T_c + T_a/2$ | $T_b + T_a/2 + T_c/2$ | $T_b + T_a + T_c/2$ |
| | $T_{K_{a2}}$ | $T_a + T_c + 2T_b/3$ | $T_a + T_b + T_c = T_m$ | $T_a + T_b + T_c = T_m$ | $T_a + T_b + T_c = T_m$ |
| | $T_{K_{b1}}$ | $T_c/2 + T_b/3$ | $0$ | $T_c/2$ | $T_a + T_c/2$ |
| | $T_{K_{b2}}$ | $T_a/2 + 2T_b/3 + T_c$ | $T_b + T_a/2$ | $T_b + T_c + T_a/2$ | $T_a + T_b + T_c = T_m$ |
| | $T_{K_{c1}}$ | $T_b/3$ | $0$ | $0$ | $0$ |
| | $T_{K_{c2}}$ | $T_a/2 + 2T_b/3 + T_c/2$ | $T_a/2$ | $T_a/2 + T_c/2$ | $T_c/2$ |
| Sector 2 | $T_{K_{a1}}$ | $T_b/3 + T_c/2$ | $T_a + T_c/2$ | $T_c/2$ | $0$ |
| | $T_{K_{a2}}$ | $T_a/2 + 2T_b/3 + T_c$ | $T_a + T_b + T_c = T_m$ | $T_a/2 + T_b + T_c$ | $T_c/2 + T_b$ |
| | $T_{K_{b1}}$ | $T_a/2 + T_b/3 + T_c/2$ | $T_a + T_b + T_c/2$ | $0$ | $T_a/2 + T_b + T_c$ |
| | $T_{K_{b2}}$ | $T_a + 2T_b/3 + T_c$ | $T_a + T_b + T_c = T_m$ | $T_a/2 + T_b + T_c/2$ | $T_a + T_b + T_c = T_m$ |
| | $T_{K_{c1}}$ | $T_b/3$ | $0$ | $T_a + T_b + T_c = T_m$ | $0$ |
| | $T_{K_{c2}}$ | $T_a/2 + 2T_b/3 + T_c/2$ | $T_c/2$ | $T_a/2 + T_c/2$ | $T_a/2$ |
| Sector3 | $T_{K_{a1}}$ | $T_b/3$ | $0$ | $0$ | $0$ |
| | $T_{K_{a2}}$ | $T_a/2 + 2T_b/3 + T_c/2$ | $T_a/2$ | $T_a/2 + T_c/2$ | $T_c/2$ |
| | $T_{K_{b1}}$ | $T_a/2 + T_b/3 + T_c/2$ | $T_a/2 + T_b + T_c$ | $T_a/2 + T_b + T_c/2$ | $T_a + T_b + T_c/2$ |
| | $T_{K_{b2}}$ | $T_a + 2T_b/3 + T_c$ | $T_a + T_b + T_c = T_m$ | $T_a + T_b + T_c = T_m$ | $T_a + T_b + T_c = T_m$ |
| | $T_{K_{c1}}$ | $T_b/3 + T_c/2$ | $0$ | $T_c/2$ | $T_a + T_c/2$ |
| | $T_{K_{c2}}$ | $T_a/2 + 2T_b/3 + T_c$ | $T_a/2 + T_b$ | $T_a/2 + T_b + T_c$ | $T_a + T_b + T_c = T_m$ |
| Sector 4 | $T_{K_{a1}}$ | $T_b/3$ | $0$ | $0$ | $T_a/2$ |
| | $T_{K_{a2}}$ | $T_a/2 + 2T_b/3 + T_c/2$ | $T_c/2$ | $T_a/2 + T_c/2$ | $0$ |
| | $T_{K_{b1}}$ | $T_b/3 + T_c/2$ | $T_a + T_c/2$ | $T_c/2$ | $T_a/2 + T_b$ |
| | $T_{K_{b2}}$ | $T_a/2 + 2T_b/3 + T_c$ | $T_a + T_b + T_c = T_m$ | $T_a/2 + T_b + T_c$ | $T_a + T_b + T_c = T_m$ |
| | $T_{K_{c1}}$ | $T_a/2 + T_b/3 + T_c/2$ | $T_a + T_b + T_c/2$ | $T_a/2 + T_b + T_c/2$ | $T_a/2 + T_b + T_c$ |
| | $T_{K_{c2}}$ | $T_a + 2T_b/3 + T_c$ | $T_a + T_b + T_c = T_m$ | $T_a + T_b + T_c = T_m$ | $T_a + T_b + T_c = T_m$ |
| Sector 5 | $T_{K_{a1}}$ | $T_b/3 + T_c/2$ | $0$ | $T_c/2$ | $T_a + T_c/2$ |
| | $T_{K_{a2}}$ | $T_a/2 + 2T_b/3 + T_c$ | $T_a/2 + T_b$ | $T_a/2 + T_b + T_c$ | $T_a + T_b + T_c = T_m$ |
| | $T_{K_{b1}}$ | $T_b/3$ | $0$ | $0$ | $0$ |
| | $T_{K_{b2}}$ | $T_a/2 + 2T_b/3 + T_c/2$ | $T_a/2$ | $T_a/2 + T_c/2$ | $T_c/2$ |
| | $T_{K_{c1}}$ | $T_a/2 + T_b/3 + T_c/2$ | $T_a/2 + T_b + T_c$ | $T_a/2 + T_b + T_c/2$ | $T_a + T_b + T_c/2$ |
| | $T_{K_{c2}}$ | $T_a + 2T_b/3 + T_c$ | $T_a + T_b + T_c = T_m$ | $T_a + T_b + T_c = T_m$ | $T_a + T_b + T_c = T_m$ |
| Sector 6 | $T_{K_{a1}}$ | $T_a/2 + T_b/3 + T_c/2$ | $T_a + T_b + T_c/2$ | $T_a/2 + T_b + T_c/2$ | $T_a/2 + T_c$ |
| | $T_{K_{a2}}$ | $T_a + 2T_b/3 + T_c$ | $T_a + T_b + T_c = T_m$ | $T_a + T_b + T_c = T_m$ | $T_a + T_b + T_c = T_m$ |
| | $T_{K_{b1}}$ | $T_b/3$ | $0$ | $0$ | $0$ |
| | $T_{K_{b2}}$ | $T_a/2 + 2T_b/3 + T_c/2$ | $T_c/2$ | $T_a/2 + T_c/2$ | $T_a/2$ |

 doi:10.20944/preprints202605.1382.v1



| | | | | | |
|---|---|---|---|---|---|
| | $T_{K_{c1}}$ | $T_b/3 + T_c/2$ | $T_a + T_c/2$ | $T_c/2$ | $T_a/2 + T_b + T_c$ |
| | $T_{K_{c2}}$ | $T_a/2 + 2T_b/3 + T_c$ | $T_a + T_b + T_c = T_m$ | $T_a/2 + T_b + T_c$ | $T_a + T_b + T_c = T_m$ |

Figure 3 illustrates the fundamental operating principles of conventional photovoltaic (PV) cells and thermoradiative (TR) cells. Under thermal equilibrium, the absorption and emission processes remain balanced. Under solar illumination, the PV cell absorbs photons with energies greater than the semiconductor bandgap, resulting in positive quasi-Fermi level splitting and electrical power generation. In thermoradiative operation, the device emits infrared photons toward a colder environment, leading to negative quasi-Fermi level splitting and nighttime electrical power generation.

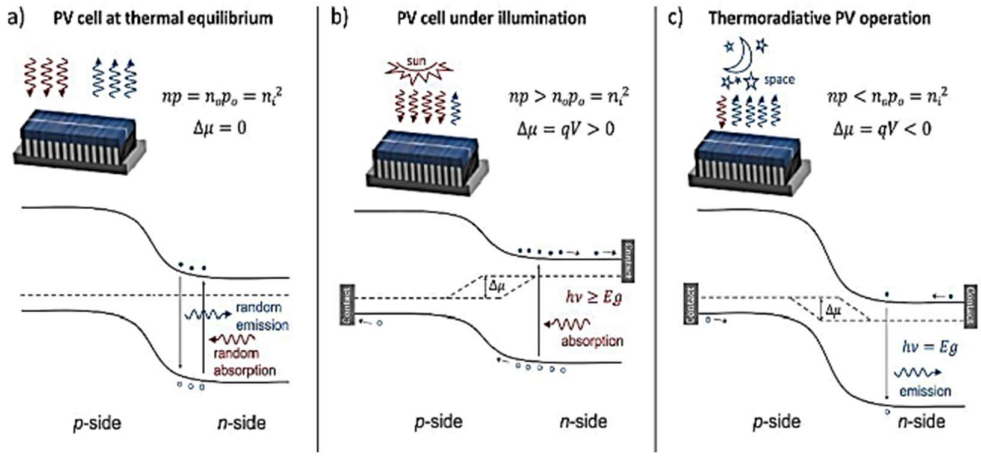


**Figure 3.** Operating principles of photovoltaic and thermoradiative cells under thermal equilibrium, illumination, and thermoradiative operation.

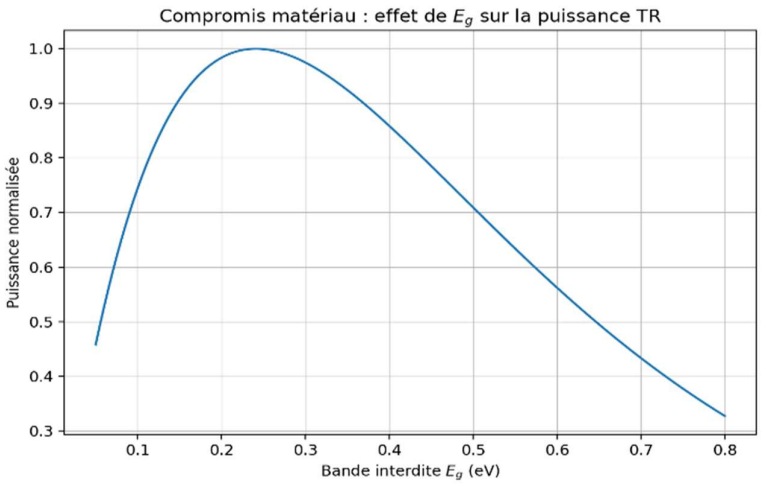


**Figure 4.** Influence of semiconductor bandgap energy on normalized thermoradiative power generation.

This figure shows the influence of the semiconductor bandgap energy $E_g$ on the normalized thermoradiative power output. The results indicate that low-bandgap materials significantly improve infrared radiative energy conversion. The maximum thermoradiative power is obtained for bandgap energies approximately between 0.1 eV and 0.3 eV, confirming the relevance of low-

 doi:10.20944/preprints202605.1382.v1



bandgap materials such as InSb and novel molecular families including SnSbX and SnAsX compounds.

Figure 5 presents the current–voltage (I–V) and power–voltage (P–V) characteristics of the photovoltaic module for different irradiation levels at constant temperature. As solar irradiance increases, both the generated current and the output power increase significantly, while the open-circuit voltage varies slightly. The maximum power point shifts upward with increasing irradiation.

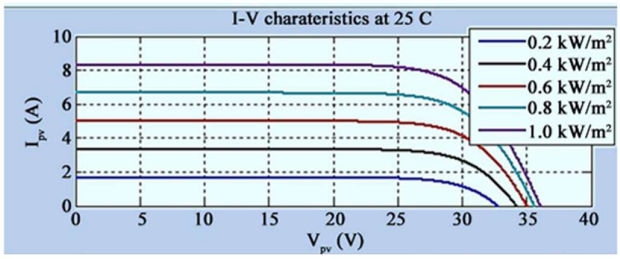


Figure 14. I-V characteristics at 25°.

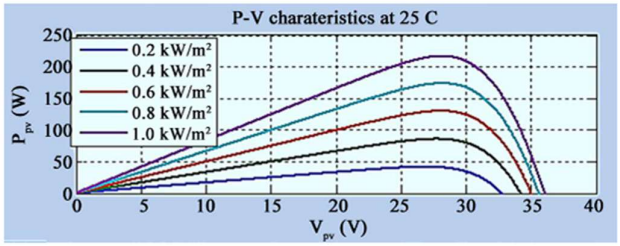


Figure 15. P-V characteristics at 25°.

**Figure 5.** I–V and P–V characteristics of the photovoltaic module under varying solar irradiance conditions at 25 °C.

Figure 6 illustrates the influence of the thermoradiative cell temperature on the normalized radiative power. The generated thermoradiative power increases significantly with temperature due to enhanced infrared photon emission. The results confirm the strong dependence of TR cell performance on thermal operating conditions.

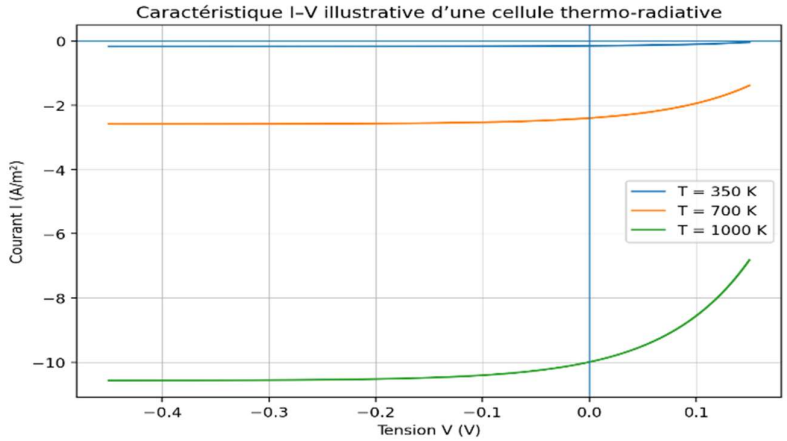


**Figure 6.** Effect of thermoradiative cell temperature on normalized radiative power generation.

 doi:10.20944/preprints202605.1382.v1



Figure 7 illustrates the nonlinear relationship between voltage, current, and generated power, highlighting the existence of a maximum power point.

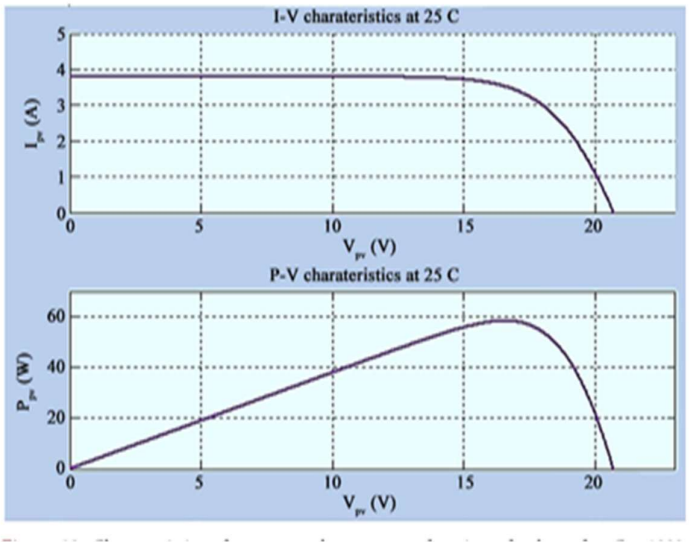


**Figure 7.** Nominal I–V and P–V characteristics of the photovoltaic module at standard operating conditions.

The obtained results demonstrate the complementary behavior of photovoltaic and thermoradiative energy conversion mechanisms. While photovoltaic systems remain highly dependent on solar irradiation and temperature conditions, thermoradiative cells provide promising nighttime energy harvesting capabilities using infrared thermal radiation. Consequently, the combination of PV, wind, and TR sources may significantly improve the continuity and stability of renewable energy supply for induction motor drive applications.

## III. Hybrid DC Bus Power Management

The hybrid renewable energy sources are interconnected through a common DC bus responsible for ensuring stable power transfer between the renewable generators, the storage system, and the induction motor drive. The DC bus plays a critical role in maintaining system stability despite the intermittent behavior of photovoltaic, wind, and thermoradiative energy sources.

The photovoltaic and thermoradiative sources are connected to the DC bus through DC/DC boost converters, while the wind energy system is connected through an AC/DC rectification stage. A bidirectional DC/DC converter is used to interface the battery storage system with the DC bus to regulate the power balance and stabilize the DC-link voltage.

Figure 8 illustrates the proposed hybrid DC bus energy management architecture supplying the induction motor drive. The photovoltaic system, thermoradiative cell, and wind energy conversion system are interconnected through a common DC bus. The photovoltaic source is regulated using an MPPT P&O controller, while the wind generator is connected through a three-phase AC/DC rectifier. The thermoradiative source is integrated through a DC/DC conversion stage.

 doi:10.20944/preprints202605.1382.v1



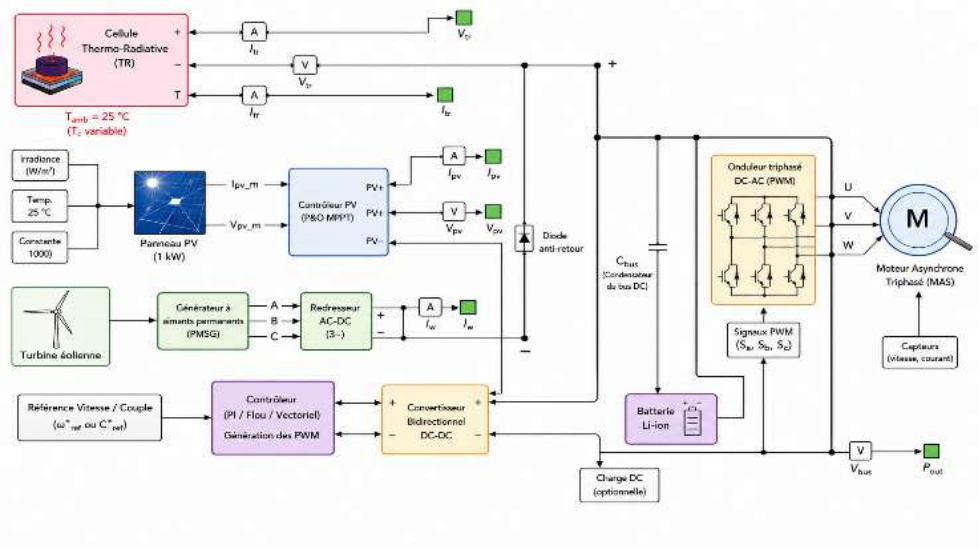


**Figure 8.** Hybrid DC bus energy management architecture for the induction motor drive system.

A bidirectional DC/DC converter interfaces the battery storage system with the DC bus to regulate the power exchange and stabilize the DC-link voltage under varying renewable generation and load conditions. The DC bus capacitor $C_{bus}$ reduces voltage fluctuations and ensures continuous power transfer toward the three-phase inverter supplying the induction motor. The generated PWM signals are obtained from the proposed control strategy (PI, Vector Control, or Fuzzy Control) to regulate the motor speed and electromagnetic torque.

The overall generated power can be expressed as:

$$P_{total} = P_{PV} + P_{wind} + P_{TR} + P_{bat}$$

where:

- $P_{PV}$ is the photovoltaic power,
- $P_{wind}$ is the wind power,
- $P_{TR}$ is the thermoradiative power,
- $P_{bat}$ is the battery exchanged power.

The DC bus voltage must remain stable under load variations and renewable source intermittency. Therefore, the battery storage system absorbs excess power during high production conditions and supplies additional energy during renewable power deficits.

The DC-link capacitor $C_{dc}$ is used to reduce voltage fluctuations and ensure smooth energy transfer toward the inverter stage. The DC bus voltage dynamics can be expressed as:

where:

- $V_{dc}$ is the DC bus voltage,
- $I_{source}$ is the total source current,
- $I_{load}$ is the inverter load current.

The stabilization of the DC bus is essential because fluctuations in $V_{dc}$ directly affect the inverter output voltages, harmonic distortion, and induction motor dynamic performance.

The regulated DC power is then supplied to the three-level inverter responsible for generating the three-phase voltages applied to the induction motor. Figure 9 presents the proposed fuzzy energy management strategy used to regulate the power exchange between the hybrid renewable sources and the battery storage system. The controller uses the difference between the renewable generated power and the load demand power as the main input variable. The battery state of charge (SOC) and the DC bus voltage are also considered in order to maintain system stability and ensure continuous power supply.

 doi:10.20944/preprints202605.1382.v1



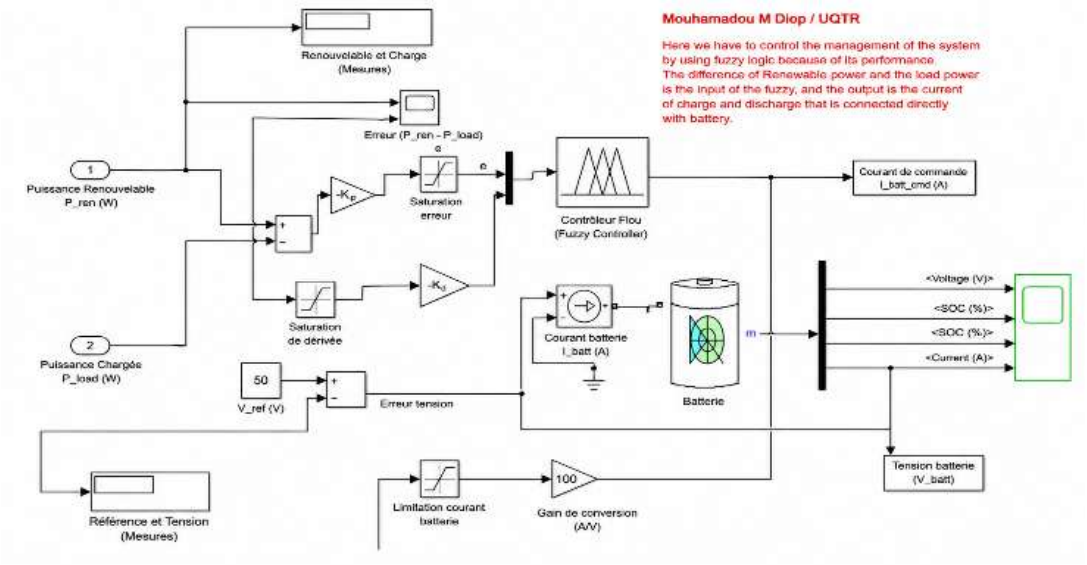


**Figure 9.** Fuzzy energy management strategy for battery charging and discharging control.

The fuzzy controller generates the reference battery current command $I_{bat\_cmd}$, which determines the charging or discharging operating mode of the battery through the bidirectional DC/DC converter.

The power balance error is defined as:

$$\Delta P = P_L - (P_{wind} + P_{PV} + P_{rad})$$

where:

- $P_L$ is the load power,
- $P_{wind}$ is the wind power,
- $P_{PV}$ is the photovoltaic power,
- $P_{rad}$ is the thermoradiative generated power.

The battery SOC error is expressed as:

$$\Delta SOC = SOC_{command} - SOC_{new}$$

Where:

- $SOC_{command}$ is the reference state of charge,
- $SOC_{new}$ the measured battery state of charge.

| **ΔI** | | **ΔP** | | | | |
|---|---|---|---|---|---|---|
| | | NB | NS | ZO | PS | **PB** |
| **ΔSOC** | NB | PB | PB | PB | PB | **PB** |
| | NS | PB | PB | PS | PS | **PB** |
| | ZO | ZO | ZO | ZO | PS | **PB** |
| | PS | NS | NS | NS | NS | **PB** |
| | **PB** | **NB** | **NB** | **NB** | **NB** | **PB** |

**Figure 10.** Fuzzy inference rules for hybrid energy management.

 doi:10.20944/preprints202605.1382.v1



Table 10 presents the fuzzy rule base used for the energy management strategy. The controller determines the battery charging or discharging current according to the power balance error $\Delta P$ and the battery state of charge error $\Delta SOC$.

Figure 11 presents the performance of the proposed DC bus energy management strategy under varying renewable generation and load conditions. The upper curve illustrates the evolution of the battery state of charge (SOC), which remains within acceptable operating limits throughout the simulation. The SOC initially increases due to excess renewable energy production and later decreases when the load demand becomes higher than the generated renewable power.

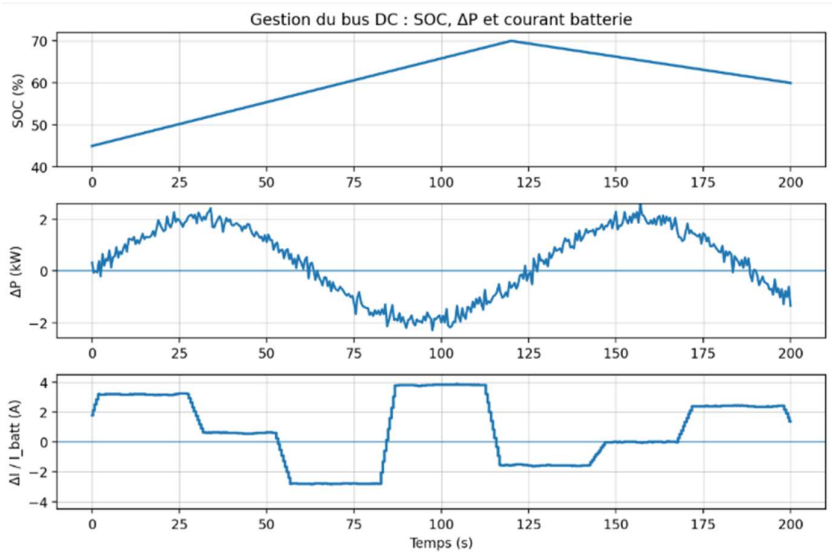


**Figure 11.** DC bus energy management results: battery SOC, power balance error, and battery current response.

The middle curve represents the power balance error $\Delta P$, defined as the difference between the load power and the total renewable generated power. Positive values of $\Delta P$ indicate surplus renewable generation, whereas negative values correspond to power deficit conditions requiring battery support.

The lower curve shows the battery current response generated by the fuzzy energy management controller. Positive battery current corresponds to battery charging operation, while negative current indicates battery discharging mode. The obtained results demonstrate that the proposed fuzzy controller effectively regulates the battery charging and discharging process to maintain DC bus stability and ensure continuous power supply to the induction motor drive system.

To improve the quality of the voltage waveform supplied to the induction motor and reduce harmonic distortion, a three-level inverter structure is adopted in this work. Compared with conventional two-level inverters, multilevel inverter topologies provide better sinusoidal approximation, lower switching stress, and reduced Total Harmonic Distortion (THD).

The obtained simulation results are presented in Figures 12 and 13.

Figure 12 presents the output phase voltages generated by the proposed three-level inverter. The inverter produces multiple voltage levels $(+200\,V,\ +100\,V, 0,\ -100\,V,\ -200\,V)$, allowing a better approximation of sinusoidal waveforms compared with conventional two-level inverter structures.

 doi:10.20944/preprints202605.1382.v1



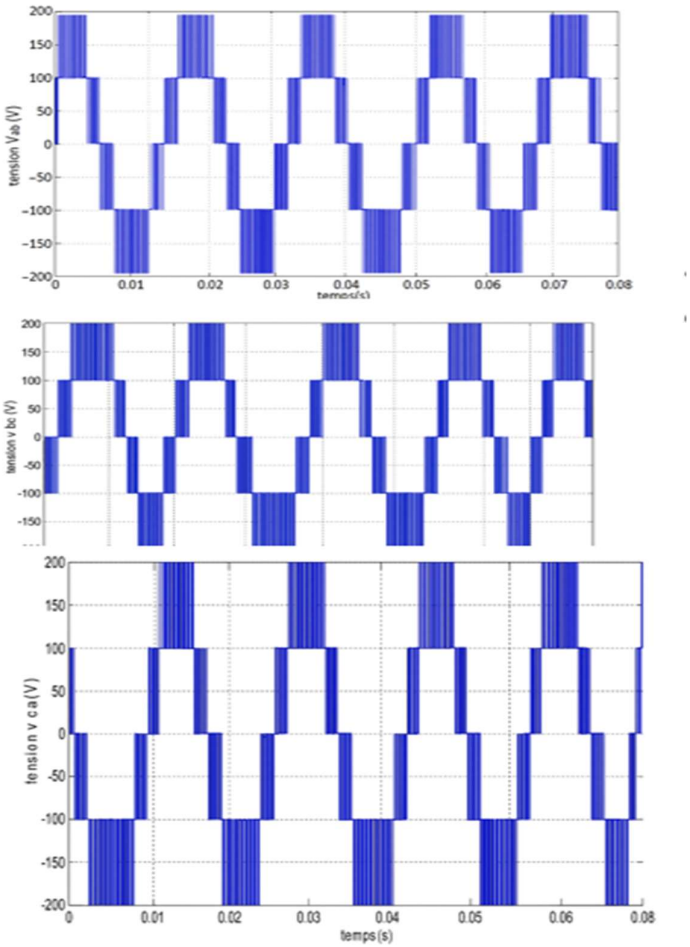


**Figure 12.** Three-level inverter output phase voltages (V.

The multilevel switching strategy significantly reduces abrupt voltage transitions and improves waveform smoothness. Consequently, the voltage stress applied to the induction motor windings is reduced, leading to improved electromagnetic performance and lower harmonic distortion.

Figure 13 illustrates the comparison between the conventional two-level inverter and the proposed three-level inverter output waveforms. The two-level inverter generates abrupt voltage transitions between positive and negative DC bus voltages, resulting in high harmonic content and increased switching stress.

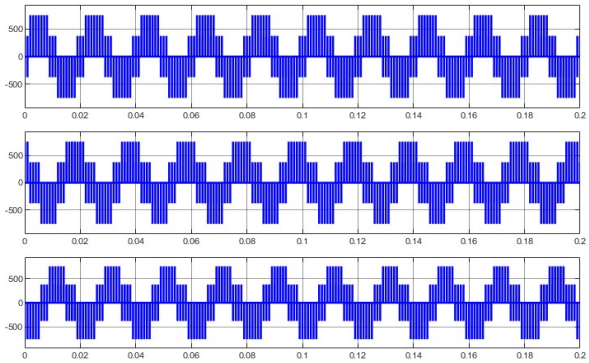

**Figure 13.** Comparison of inverter output voltages between two-level and three-level inverter structures.

 doi:10.20944/preprints202605.1382.v1



In contrast, the three-level inverter introduces intermediate voltage levels, producing a staircase waveform closer to an ideal sinusoidal signal. This improvement reduces the harmonic content of the output voltage and enhances the quality of the stator currents supplied to the induction motor.

The comparison clearly demonstrates that the three-level inverter offers several advantages over the conventional two-level structure, including:

- lower Total Harmonic Distortion (THD),
- Reduced switching losses,
- smoother voltage transitions,
- improved current waveform quality,
- reduced electromagnetic stress on the machine,
- improved dynamic behavior of the induction motor drive.

The reduction of voltage harmonics directly contributes to minimizing stator current ripple and improving the overall efficiency of the proposed hybrid renewable energy conversion system.

The main parameters of the proposed hybrid renewable energy system, induction motor drive, multilevel inverter, battery storage system, and ALFQ controller used in the MATLAB/Simulink simulations are summarized in Table 4.

**Table 4.** Main parameters of the proposed hybrid renewable energy induction motor drive system and ALFQ controller.

| System Component | Parameter | Value |
|---|---|---|
| Induction Motor (IM) | Rated Power | 1.5 kW |
| Induction Motor (IM) | Rated Voltage | 400/230 V |
| Induction Motor (IM) | Frequency | 50 Hz |
| Induction Motor (IM) | Stator Resistance (Rs) | 2.475 Ω |
| Induction Motor (IM) | Rotor Resistance (Rr) | 4.446 Ω |
| Induction Motor (IM) | Stator Inductance (Ls) | 270.315 mH |
| Induction Motor (IM) | Rotor Inductance (Lr) | 270.315 mH |
| Induction Motor (IM) | Mutual Inductance (Lm) | 259.836 mH |
| Induction Motor (IM) | Pole Pairs (p) | 1 |
| Induction Motor (IM) | Rotor Inertia (J) | 0.023 kg·m² |
| Induction Motor (IM) | Friction Coefficient (fr) | $26 \times 10^{-4}$ |
| Photovoltaic System (PV) | Rated Power | 1 kW |
| Photovoltaic System (PV) | Standard Irradiance | 1000 W/m² |
| Photovoltaic System (PV) | Operating Temperature | 25 °C |
| Wind Energy System | Nominal Mechanical Output Power | 5 kW |
| Wind Energy System | Base Generator Power | 190/9 VA |
| Wind Energy System | Base Wind Speed | 12 m/s |

 doi:10.20944/preprints202605.1382.v1



| | | |
|---|---|---|
| Wind Energy System | Maximum Power Coefficient (Cp) | 0.73 |
| Wind Energy System | Base Rotational Speed | 1.2 p.u |
| Wind Energy System | Pitch Angle β | 0° |
| Thermoradiative Cells (TR) | Energy Contribution | 25% of PV power |
| Thermoradiative Cells (TR) | Semiconductor Bandgap (Eg) | 0.1–0.3 eV |
| Thermoradiative Cells (TR) | Candidate Materials | InSb, SnSbX, SnAsX |
| Battery Storage System | Battery Type | Lithium-Ion |
| Battery Storage System | Nominal Voltage | 24 V |
| Battery Storage System | Rated Capacity | 100 Ah |
| Battery Storage System | Initial State of Charge (SOC) | 80% |
| Battery Storage System | Battery Response Time | 70 s |
| DC Bus | DC-Link Voltage (Vdc) | 565 V |
| DC Bus | DC Bus Capacitor (Cdc) | 2200 μF |
| Multilevel Inverter | Topology | Three-Level Inverter |
| Multilevel Inverter | Output Voltage Levels | ±200 V, ±100 V, 0 |
| Multilevel Inverter | PWM Technique | Sinusoidal PWM |
| ALFQ Controller | Optimization Objective | MAE minimization |
| ALFQ Controller | Membership Functions | 7 triangular MFs |
| ALFQ Controller | Controller Inputs | Speed error (e), change of error (Δe) |
| ALFQ Controller | Optimization Method | Quantum-inspired optimization |

## IV. Proposed Adaptive Quantum Fuzzy Logic (ALFQ) Controller

The proposed Adaptive Quantum Fuzzy Logic (ALFQ) controller combines the robustness of classical fuzzy logic with the optimization capability of quantum-inspired search algorithms. Unlike conventional Fuzzy Logic Controllers (FLC), where the membership functions are fixed and manually tuned, the ALFQ controller dynamically optimizes the membership functions using a quantum search mechanism.

The objective of the proposed method is to minimize the speed tracking error while improving the dynamic behavior of the induction motor drive supplied by the hybrid renewable energy system.

The ALFQ controller uses:

- the speed error $e$,
- the change of error $\Delta e$,

as input variables, while the controller output generates the electromagnetic control action applied to the induction motor drive.

The optimization process continuously adjusts the membership function parameters to minimize the Mean Absolute Error (MAE) between the reference speed and the actual motor speed.

 doi:10.20944/preprints202605.1382.v1



The quantum search algorithm is inspired by probabilistic quantum mechanics behavior. In the proposed approach, each particle represents a possible solution corresponding to a set of fuzzy membership function parameters.

The stochastic attractor position of each particle is expressed as:

$$P_{ij}^{t} = \frac{a_{ij}^{t} P_{ij,best}^{t} + b_{ij}^{t} Gsl_{ij}^{t}}{c_{ij}^{t} SF}$$

Where:

- $P_{ij}^{t}$ represents the current particle position,
- $P_{ij,best}^{t}$ is the best local position of the particle,
- $Gsl_{ij}^{t}$ is the best global solution,
- $a$, $b$, and $c$ are uniformly distributed random numbers,
- $SF$ is the scaling factor.

The quantum behavior of each particle is represented through a wave function given by:

$$\psi(P_{ij}^{t+1}) = \frac{1}{\sqrt{L_{ij}^{t}}} \exp\left(\frac{P_{ij}^{t}}{L_{ij}^{t}}\right)$$

The parameter $L_{ij}^{t}$ represents the characteristic length of the quantum particle and is expressed as:

$$L_{ij}^{t} = 2\beta \mid Mbest_{j}^{t} - P_{ij}^{t} \mid$$

Where:

- $\beta$ is the contraction–expansion coefficient,
- $Mbest_{j}^{t}$ is the mean best position of all particles.

The mean best position is calculated by:

$$Mbest_{j}^{t} = \frac{1}{N} \sum_{j=1}^{D} P_{ij}^{t}$$

The contraction–expansion coefficient evolves during the optimization process according to:

$$\beta = \beta_0 + (T - t)\frac{\beta_1 - \beta_0}{T}$$

This adaptive coefficient controls the balance between exploration and exploitation during the optimization process.

The ALFQ controller optimizes the fuzzy membership functions associated with:

- speed error,
- change of error,
- controller output.

 doi:10.20944/preprints202605.1382.v1



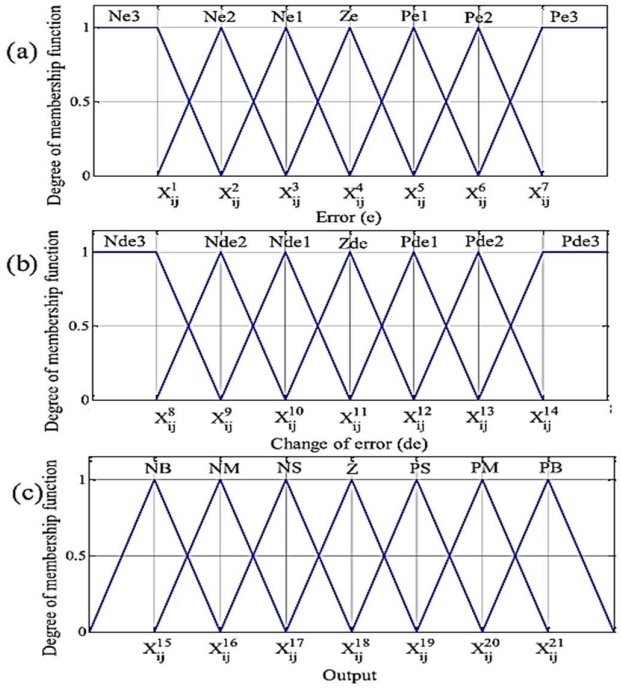


**Figure 14.** Optimization of Fuzzy Membership Functions.

The fuzzy inference system uses seven triangular membership functions for each variable:

- NB: Negative Big,
- NM: Negative Medium,
- NS: Negative Small,
- Z: Zero,
- PS: Positive Small,
- PM: Positive Medium,
- PB: Positive Big.

The optimized membership function parameters are organized in the matrix:

$$D_{ij} = \begin{bmatrix} X_{11} & \cdots & X_{1j} \\ \vdots & \ddots & \vdots \\ X_{i1} & \cdots & X_{ij} \end{bmatrix}$$

Each particle of the quantum optimizer therefore represents a complete set of membership function coordinates defining the fuzzy controller behavior.

The optimization objective is based on minimizing the Mean Absolute Error (MAE) between the reference speed and the actual rotor speed:

$$MAE = \frac{1}{l}\sum_{m=1}^{M} \mid \omega_{rm}^{*} - \omega_{rm} \mid$$

where:

- $\omega_{rm}^{*}$is the reference rotor speed,
- $\omega_{rm}$is the measured rotor speed,
- $M$is the number of samples.

 doi:10.20944/preprints202605.1382.v1



The minimization of MAE improves:

- tracking precision,
- dynamic response,
- disturbance rejection,
- system stability.

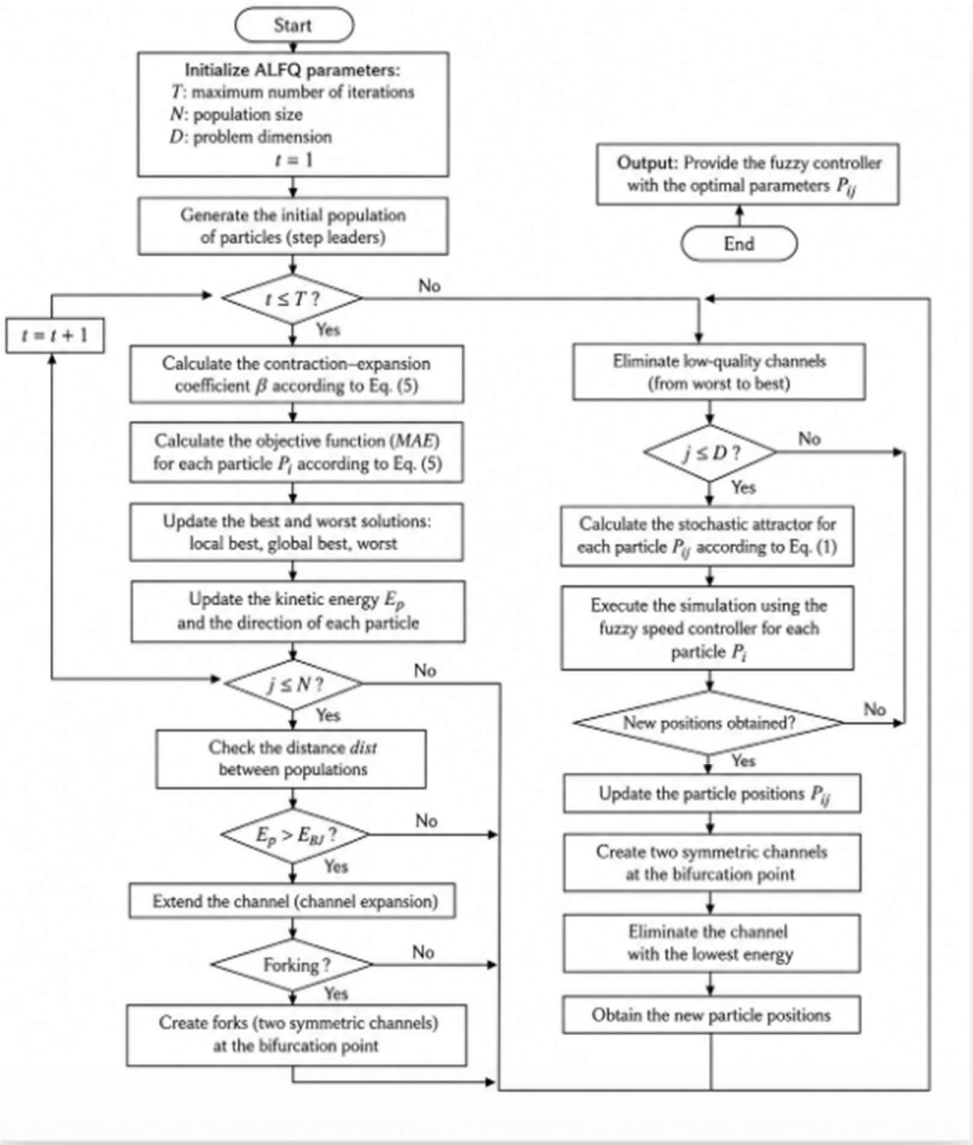


**Figure 15.** ALFQ Optimization Algorithm.

The complete optimization process of the proposed ALFQ controller is summarized by the flowchart shown in Fig. XX.

Initially, the optimization parameters are defined, including:

- maximum number of iterations $T$,
- particle population size $N$,
- optimization dimension $D$.

An initial population of particles is randomly generated, where each particle represents a possible configuration of the fuzzy membership functions.

For each iteration:

1. The contraction–expansion coefficient $\beta$is updated.

 doi:10.20944/preprints202605.1382.v1



2. The objective function (MAE) is calculated.
3. The best local and global particle positions are updated.
4. The stochastic attractor is computed.
5. The fuzzy speed controller simulation is executed.
6. The particle positions are updated according to the quantum optimization equations.
7. Low-energy channels are eliminated while better solutions are preserved.

The optimization process continues until the stopping criterion is reached.

Finally, the optimal fuzzy membership functions are obtained and used in the induction motor control system.

## IV. Results and Performance Analysis of the Proposed ALFQ Controller

Figures 16 and 17 present the dynamic speed response and stator current behavior of the induction motor controlled by the proposed Adaptive Quantum Fuzzy Logic (ALFQ) strategy under no-load and load conditions, respectively.

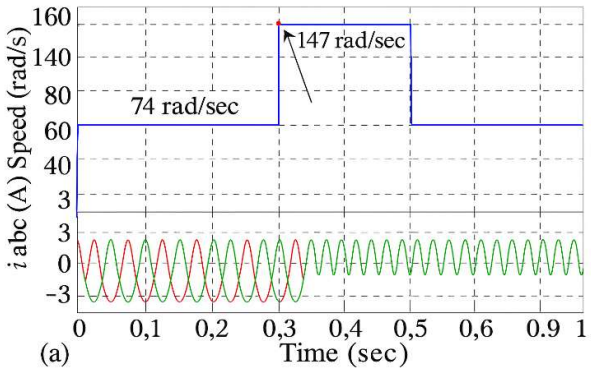


**Figure 16.** Step speed response and stator currents of the induction motor during the speed transition from 74 to 147 rad/s: (a) no-load simulation.

**Table 5.** Dynamic performance indicators of the proposed ALFQ controller under no-load speed transition conditions.

| Indicateurs | Signification | Valeurs |
|---|---|---|
| **ω1 (rad/s)** | Niveau de vitesse bas | 74 |
| **ω2 (rad/s)** | Niveau de vitesse haut | 147 |
| **Δω (rad/s)** | Amplitude du saut de consigne | 73 |
| **t_step↑ (s)** | Instant du saut 74→147 | ≈ 0.30 s |
| **t_step↓ (s)** | Instant du retour (147→niveau bas) | ≈ 0.50 s |
| **t_r (s)** | Temps de montée (≈10–90%) | ≈ 0.02–0.03 s |
| **M_p (%)** | Dépassement relatif sur la vitesse | ≈ 0% |
| **e_ss (%)** | Erreur statique | ≈ 0% (superposition consigne/sortie) |

 doi:10.20944/preprints202605.1382.v1



In the first test case shown in Figure 16 and Tab 5, the reference speed changes from $74$ rad/sto 147 rad/sat approximately $t = 0.30\ s$, before returning to the initial speed at $t = 0.50\ s$. The obtained results demonstrate a very fast dynamic response with a rise time of approximately $0.02–0.03\ s$. The motor speed perfectly tracks the reference signal without observable overshoot, yielding an estimated overshoot $M_p \approx 0\%$and negligible steady-state error.

The three-phase stator currents remain balanced and quasi-sinusoidal during the transient operation. Only a slight temporary increase in current amplitude is observed during acceleration due to the additional electromagnetic torque required for speed increase.

**Table 6.** Dynamic performance indicators of the proposed ALFQ controller under load speed transition conditions.

| Indicateurs | Signification | Valeurs |
|---|---|---|
| **ω1 (rad/s)** | Niveau de vitesse bas | 74 |
| **ω2 (rad/s)** | Niveau de vitesse haut | 147 |
| **t_step↑ (s)** | Instant du saut 74→147 | ≈ 0.20–0.22 s |
| **t_step(s)** | Instant du retour (147→niveau intermédiaire) | ≈ 0.50 s |
| **t_s (s)** | Temps d'établissement (±2%) après saut | ≈ 0.03–0.05 s |
| **M_p (%)** | Dépassement relatif | ≈ 0% |
| **I_p (A)** | Pic de courant statorique au régime 50 Hz | ≈ 2.2 A |
| **I_p (A)** | Pic de courant statorique au régime 25 Hz | ≈ 2.0 A |

The second test case presented in Figure 17 and tab6 evaluates the controller performance under load conditions. The reference speed transition occurs between $74$ rad/sand $147$ rad/s, with a settling time approximately between $0.03$and $0.05\ s$. Despite the load application, the proposed ALFQ controller maintains stable operation and excellent speed tracking capability.

The peak stator current reaches approximately:

- $I_p \approx 2.2\ A$at $50\ Hz$,
- $I_p \approx 2.0\ A$at $25\ Hz$,

while preserving smooth current waveforms and low oscillatory behavior.

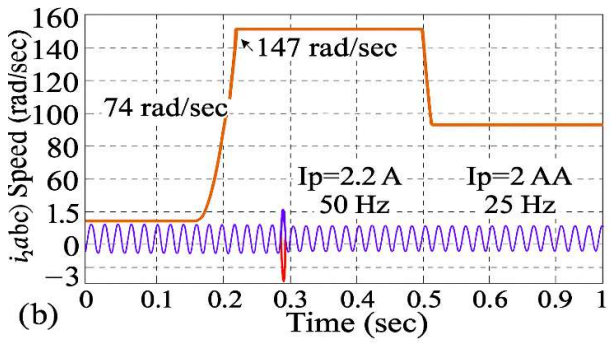


**Figure 17.** Step speed response and stator currents of the induction motor during the speed transition from 74 to 147 rad/s: (b) loaded simulation

 doi:10.20944/preprints202605.1382.v1



**Table 7.** Dynamic performance indicators of the proposed ALFQ controller under no-load ramp speed conditions.

| Indicateurs | Signification | Valeurs |
|---|---|---|
| **ω_min (rad/s)** | Vitesse minimale atteinte | ≈ 74 |
| **ω_max (rad/s)** | Vitesse maximale atteinte | ≈ 147 |
| **Suivi rampe** | Capacité à suivre une consigne variable | Bon suivi (écart faible visible) |
| **Ondulation ω** | Ripple de vitesse pendant rampe | Faible (pas d'oscillation marquée) |
| **i_abc (A)** | Amplitude typique des courants statoriques | ≈ ±2 à ±3 A |

Figure 18 and Tab7 present the ramp speed response and the corresponding three-phase stator currents of the induction motor controlled by the proposed Adaptive Quantum Fuzzy Logic (ALFQ) strategy under no-load conditions. The reference speed progressively varies between approximately $74\ \text{rad/s}$ and $147\ \text{rad/s}$, allowing evaluation of the controller performance under continuously changing operating conditions.

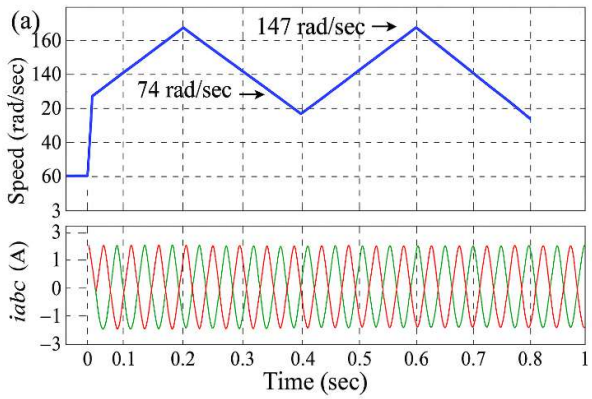


**Figure 18.** Ramp speed response and stator currents of the induction motor during the speed variation from 74 to 147 rad/s: (a) no-load operation.

The obtained results demonstrate that the proposed ALFQ controller ensures excellent ramp tracking capability with smooth transient behavior and negligible tracking error. The rotor speed accurately follows the reference trajectory without noticeable oscillations or instability during both acceleration and deceleration phases.

The stator currents $i_{abc}$ remain balanced and quasi-sinusoidal throughout the simulation, confirming the good electromagnetic behavior of the proposed controller. The current amplitude remains approximately within the range of $\pm 2$ to $\pm 3\ A$, indicating stable energy conversion and reduced current ripple during speed variation.

Table 3 summarizes the main dynamic performance indicators obtained under no-load ramp operating conditions. The minimum and maximum rotor speeds are approximately $74\ \text{rad/s}$ and $147\ \text{rad/s}$, respectively. The obtained results confirm good ramp-following capability with very low visible tracking error and reduced speed ripple.

 doi:10.20944/preprints202605.1382.v1



**Table 8.** Dynamic performance indicators of the proposed ALFQ controller under loaded ramp speed conditions.

| Indicateurs | Signification | Valeurs |
|---|---|---|
| **Charge (N·m)** | Couple résistant appliqué | 3.2 N·m |
| **ω_min (rad/s)** | Vitesse minimale atteinte | ≈ 74 (annoté) |
| **ω_max (rad/s)** | Vitesse maximale atteinte | ≈ 147 (annoté) |
| **Robustesse charge** | Maintien du suivi malgré charge | Bon (stable) |
| **Perturbation courant** | Transitoire courant lors du changement | Pic local visible (court) |
| **i_abc (A)** | Amplitude des courants en régime transitoire | ≈ ±2 à ±3 A |

Figure 19 and tab 8 show the ramp speed response and the stator currents of the induction motor under the proposed ALFQ controller without load. The motor speed successfully follows the reference ramp from $74\ \mathrm{rad/s}$ to $147\ \mathrm{rad/s}$ with smooth behavior and without significant oscillations. The three-phase stator currents remain balanced and quasi-sinusoidal during the entire simulation.

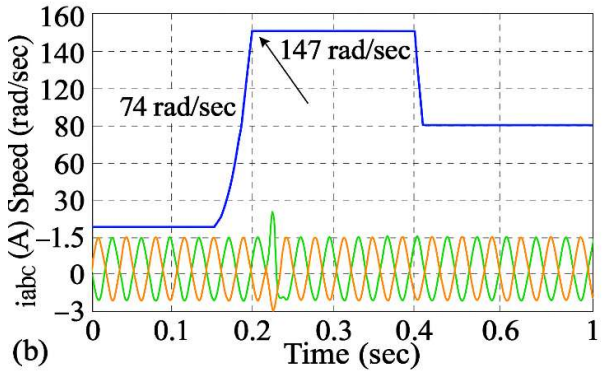


**Figure 19.** Ramp speed response and stator currents of the induction motor during the speed variation from 74 to 147 rad/s: (b) loaded operation with a 3.2 N·m load torque.

Table 4 summarizes the main dynamic performance indicators obtained during the ramp speed test. The results confirm good tracking capability, low speed ripple, and stable current amplitude between approximately $\pm 2$and $\pm 3\ A$. These results demonstrate the effectiveness of the proposed ALFQ controller under variable speed operating conditions.

Based on the literature review and the obtained simulation results, a comparative analysis between Vector Control (VC), classical Fuzzy Logic Control (FLC), and the proposed Adaptive Quantum Fuzzy Logic (ALFQ) controller was carried out in Tab 9. The comparison highlights the advantages and

limitations of each control strategy in terms of dynamic response, robustness, harmonic distortion, tracking capability, and sensitivity to parameter variations.

The obtained results demonstrate that conventional Vector Control provides satisfactory performance under nominal operating conditions but remains highly sensitive to machine parameter variations, particularly rotor resistance changes. Classical Fuzzy Logic Control improves robustness and disturbance rejection; however, its performance still depends on heuristic tuning procedures.

 doi:10.20944/preprints202605.1382.v1



In contrast, the proposed ALFQ controller exhibits superior overall performance, including faster response time, negligible overshoot, improved robustness, lower current ripple, and reduced THD. The integration of quantum optimization mechanisms allows automatic adjustment of the fuzzy membership functions, significantly enhancing system adaptability and stability under varying operating conditions.

**Table 9.** Comparative analysis of Vector Control, Fuzzy Logic Control, and the proposed Adaptive Quantum Fuzzy Logic strategy for induction motor drives.

| **Comparison Criteria** | **Vector Control (VC)** | **Fuzzy Logic Control (FLC)** | **Adaptive Quantum Fuzzy Logic (ALFQ)** |
|---|---|---|---|
| Operating Principle | Accurate mathematical model and flux–torque decoupling | Heuristic fuzzy rules | Fuzzy logic optimized using quantum algorithm |
| Dependence on Machine Parameters | Very high | Low | Very low |
| Sensitivity to Rotor Resistance (Rr) | High | Moderate | Very low |
| Robustness Against Disturbances | Moderate | Good | Very high |
| Response Time | Fast | Medium | Very fast |
| Dynamic Overshoot | Significant | Reduced | Quasi-zero |
| Steady-State Error | Present under load | Low | Negligible |
| Speed Tracking | Good under nominal conditions | Good | Very accurate |
| Ramp Tracking | Sensitive to variations | Acceptable | Highly efficient |
| Flux–Torque Decoupling | Efficient but fragile | Improved | Very stable |
| Current/Torque Ripple | High | Reduced | Very low |
| Stator Currents | Distorted under disturbances | More stable | Quasi-sinusoidal |
| Current THD | High | Medium | Very low |
| Nonlinearity Management | Limited | Good | Excellent |
| Load Disturbance Rejection | Moderate | Good | Excellent |
| Adaptability | Low | Medium | Very high |
| Design Complexity | High | Medium | High |
| Optimization Method | Fixed parameters | Heuristic tuning | Automatic MF optimization |
| Global Stability | Moderate | Good | Very high |
| Overall Performance | Good | Very good | Excellent |

 doi:10.20944/preprints202605.1382.v1



## V. Conclusion

This paper presented a comparative analysis of Vector Control (VC), classical Fuzzy Logic Control (FLC), and the proposed Adaptive Quantum Fuzzy Logic (ALFQ) controller for induction motor drives supplied by a hybrid renewable energy system composed of photovoltaic panels, wind energy, thermoradiative cells, and battery storage connected to a common DC bus.The obtained results demonstrated that the proposed ALFQ controller significantly improves the dynamic performance of the induction motor compared with conventional VC and FLC approaches. The proposed strategy ensures faster response time, quasi-zero overshoot, reduced current ripple, lower THD, and improved robustness against load disturbances and parameter uncertainties. The integration of quantum-inspired optimization mechanisms also enables automatic tuning of the fuzzy membership functions, enhancing system adaptability and stability.

As future work, Digital Twin technology will be integrated within the proposed system for real-time monitoring and predictive maintenance purposes in the Industry 4.0 framework. The future Digital Twin architecture will combine electrical, thermal, ANFIS, and finite element models to estimate losses, efficiency degradation, and fault evolution of the induction motor using real-time operational data. This approach aims to enable intelligent fault diagnosis, remaining useful life (RUL) estimation, and predictive maintenance of high-performance electrical drive systems.

**Acknowledgments:** The authors would like to express their sincere gratitude to the members of the LGÉT-UQTR laboratory for their technical support, scientific discussions, and valuable collaboration throughout this research work. Special thanks are addressed to Prof. Adam W. Skorek for his guidance, expertise, and continuous support in the development of this study.

## References

1. M. M. Diop, A. W. Skorek, and A. Diop, “The limits of low efficiency of thermoradiative cells and its design with chemical molecules,” *World Acad. Sci. Eng. Technol.*, vol. 20, no. 5, pp. 1–10, May 2026.
2. Y. Lin, B. Zhao, and S. Fan, “Theory of thermal radiation energy conversion through thermoradiative cells,” *J. Appl. Phys.*, vol. 122, no. 24, Dec. 2017.
3. Y. Lin and T. Liao, “Thermoradiative devices for low-grade heat energy conversion,” *IEEE Trans. Electron Devices*, vol. 67, no. 3, pp. 1132–1135, Mar. 2020.
4. J. Phillips, “Thermoradiative energy conversion for infrared harvesting,” *IEEE Trans. Electron Devices*, vol. 68, no. 2, pp. 928–930, Feb. 2020.
5. T. Liao, Y. Lin, and S. Fan, “Thermoradiative energy conversion using low bandgap materials,” *IEEE Trans. Electron Devices*, vol. 66, no. 3, pp. 1386–1389, Mar. 2019.
6. W.-C. Hsu *et al.*, “Entropic and near-field improvements of thermoradiative cells,” *Sci. Rep.*, vol. 6, 2016.
7. N. Pokharel *et al.*, “Development of low-bandgap In(As)Sb thermoradiative cells for space applications,” in *Proc. IEEE Photovolt. Spec. Conf. (PVSC)*, 2025.
8. W. Deng and S. Zuo, “Comparative study of sideband electromagnetic force in internal and external rotor PMSMs with SVPWM technique,” *IEEE Trans. Ind. Electron.*, vol. 66, no. 2, pp. 956–966, Feb. 2019.
9. S. M. Mirić *et al.*, “Enhanced complex space vector modeling and control system design of multiphase magnetically levitated rotary–linear machines,” *IEEE J. Emerg. Sel. Topics Power Electron.*, vol. 8, no. 2, pp. 1833–1849, Jun. 2020.
10. G. Sala *et al.*, “Post-fault operation of bearingless multisector SPM machines by space vector control,” *IEEE Trans. Power Electron.*, vol. 35, no. 4, pp. 4168–4177, Apr. 2020.
11. H. M. Mzungu, A. B. Sebitosi, and M. A. Khan, “Comparison of standards for determining losses and efficiency of three-phase induction motors,” in *Proc. IEEE PowerAfrica Conf.*, Johannesburg, South Africa, Jul. 2007, pp. 1–6.
12. A. Goroshko, M. Zembytska, and V. Paiuk, “Induction motor vibrations caused by rotor mechanical and magnetic eccentricity,” *J. Eng. Sci.*, vol. 11, pp. D66–D77, 2024.

 doi:10.20944/preprints202605.1382.v1



13. V. Malyar, "Mathematical modeling in phase coordinates of starting modes and static characteristics of a wound-rotor induction motor," *Przeglad Elektrotechniczny*, vol. 1, pp. 116–121, 2023.
14. M. A. B. Siddique, D. Zhao, A. U. Rehman, K. Ouahada, and H. Hamam, "An adapted model predictive control MPPT for validation of optimum GMPP tracking under partial shading conditions," *Sci. Rep.*, vol. 14, no. 1, Art. no. 9462, 2024.